Accurate "metal pre-buried" strategy for constructing Ni–N$_2$C$_2$ single-atom sites with high metal loadings toward electrocatalytic CO$_2$ reduction

Xian Liu, [a] Luliang Liao, [b] Guoming Xia, [b] Fuqing Yu, [a] Guangyao Zhang, [a] Minxing Shu [a] and Hongming Wang*[a, b]

[a] College of Chemistry and Chemical Engineering, Nanchang University, Nanchang 330031, China.

[b] Institute for advanced Study, Nanchang University, Nanchang 330031, China.

Experimental Section.

1. Catalyst Synthesis.

1.1 Synthesis of 3,3'-dialdehyde-4,4'-dihydroxybiphenyl: [1]

4,4'-dihydroxybiphenyl (4 g, 21.48 mmol) and hexamethylenetetramine (6.06 g, 42.96 mmol) were mixed in a 500-mL round-bottom flask followed by the addition of anhydrous trifluoroacetic acid (150 mL). The resulting mixture was stirred at 70 °C under a N_2 atmosphere for 3 h. After pouring a certain amount of cold distilled water, the mixture was stirred for another 3 h at room temperature to obtain a yellow solid, which was extracted with ethyl acetate (3 × 50 mL) after filtering. The produced organic solution was dried over Na_2SO_4 and evaporated. The crude product was purified by column chromatography (silica gel, petroleum ether: ethyl acetate = 10: 1) to obtain a light-yellow solid, which was subsequently dried under vacuum with a yield of 2.1 g, 42%. ^{1}H NMR (400 MHz, $CDCl_3$, δ):11.03 (s, 1H), 10.00 (s, 1H), 7.74 (d, J = 6.40 Hz, 2H), 7.11 (d, J = 9.26 Hz, 1H) (Fig. S1).

1.2 Synthesis of Ni-salen crystalline polymer:[2]

1,2,4,5-benzene tetramine tetrahydrochloride (59.0 mg, 0.208 mmol) was dispersed in a mixture of 1,3,5-trimethylbenzene and ethanol solvents with a ratio of 2:1 (8, 4 mL) inside a 50-mL hydrothermal synthesis reactor. Triethylamine (120 μL, 0.832 mmol) was added to the mixture, which was sonicated for 5 min. Next, $Ni(OAc)_2 \cdot 4H_2O$ (102.88 mg, 0.416 mmol), 3,3'-dialdehyde-4,4'-dihydroxybiphenyl (100 mg, 0.416 mmol), and aqueous solution of acetic acid (1 mL, 6.0 m) were added to the hydrothermal synthesis reactor, and the resulting mixture was sonicated for another 5 min. Finally, the mixture was heated to 80 °C for 5 d to synthesize a reddish-brown solid, which was filtered and washed with ultrapure water, anhydrous ethanol, tetrahydrofuran, and acetone, and then dried at 160 °C under vacuum for 12 h to obtain a reddish-brown powder.

1.3 Fabrication of electrocatalysts

First, sodium citrate (8 mmol) was pyrolyzed at 800 °C for 1 h in a tube furnace under an Ar atmosphere. The black solid product was washed with an HCl solution (0.5 m) and ultrapure water to remove inorganic impurities. After drying at 70 °C, a PC support was obtained. Next, PC (10 mg), dicyandiamide (125 mg), and Ni-salen crystalline polymer (50 mg) were added to the mortar and ground for 30 min. The obtained powder was placed in a tube furnace and heated to 650 °C

under an Ar flow (100 mL min^{-1}). After 200 min of pyrolysis, Ni–NC-50 was produced. Similarly, the Ni–NC-10, Ni–NC-20, Ni–NC-30, and Ni–NC-40 catalysts were fabricated by varying the content of Ni-salen crystalline polymer. The metal-free NC was synthesized using a procedure similar to that utilized for Ni–NC preparation, except for employing Ni-salen polymer as the precursor.

2. Material characterization

The powder XRD patterns were collected on a SmartLab 9 kW instrument using Cu Kα radiation. The SEM images were obtained using a field emission environmental scanning electron microscope (Quanta 200FEG). The TEM images were obtained on a JEM–2100 microscope at an acceleration voltage of 200 kV. The HAADF–STEM observations were performed using an FEI Themis Z instrument. An Agilent ICPOES730 ICP atomic emission spectrometer was used to quantify Ni contents. The XPS profiles of the studied materials were acquired using a Thermo Scientific K-Alpha instrument equipped with an Al-Kα radiation source. FT-IR spectra were recorded with a TENSOR II FT-IR instrument. Nitrogen sorption measurements were conducted at 77 K using a Micromeritics ASAP2460 system. The Raman spectra were recorded on a Renishaw Invia instrument equipped with two edge Rayleigh filters and an interference filter for plasma line removal. The synchrotron radiation experiment was performed at the BL08B2* beamline of SPring synchtron radiation facility (8 GeV, 100 mA), Japan, in which, the X-ray beam was monochromatized with a water-cooled Si (111) double-crystal monochromator and focused around the sample position using two Rh-coated focusing mirrors with beam sizes of 2.0 mm in the horizontal direction and 0.5 mm in the vertical direction.

3. Electrochemical measurements

The CO_2RR performance of the analyzed materials was evaluated on a three-electrode system using a Ag/AgCl electrode as the reference electrode, graphite as the counter electrode, and a $KHCO_3$ solution (0.5 M) as the electrolyte. The working electrode was fabricated by evenly applying a catalyst ink onto carbon paper (1×1 cm). The catalyst ink was prepared by dispersing a catalyst (0.5 mg) in ethanol (0.5 mL) containing Nafion (20 μL, 5 wt.%) and sonicated for 1 h. $KHCO_3$ solution (35 mL, 0.5 M) was added to the cathode and anode compartments of the

electrolytic cell, and high-purity CO_2 was passed through the cathode compartment at a rate of 20 mL^{-1} min for at least 30 min to obtain a CO_2-saturated electrolyte. All potentials reported in this work were converted from vs. Ag/AgCl to vs. RHE by adding a value of 0.197 + 0.059 × pH. All electrochemical tests were performed on a CHI 760e electrochemical workstation (Chenhua, Shanghai). The LSV measurements were conducted at a scan rate of 5 mV s^{-1} in a KHCO$_3$ solution (0.5 M). The ECSAs of the prepared catalysts were compared by measuring their double layer capacitances calculated from the corresponding cyclic voltammetry curves in the potential window from −0.05 to 0.05 V vs. RHE. The EIS experiments for CO_2 reduction at the open-circuit potential were performed at a small (5 mV) AC voltage in a frequency range from 10 mHz to 100 KHz.

The flow cell system was fabricated with a CO_2 gas compartment and two liquid compartments with channels. An anion exchange membrane (Fumasep FAB-PK-130) was employed to separate the anolyte and catholyte chambers. A Ni-NC-50 loaded gas diffusion layer (GDL, SGL Sigracet 22 BB, 3 cm × 1.5 cm, working area: 2 × 0.5, loading ~0.2 mg cm^{-2}) was prepared as working electrode. A Pt sheet and Ag/AgCl electrodes were used as the counter electrode and the reference electrode. 1 M aqueous KOH solution was circulated into both the anode and cathode chambers at a constant flow rate of 20 ml min^{-1} with the assistance of a dual-channel peristaltic pump. A high-purity CO_2 gas flow of 20 cm^3 min^{-1} was supplied to the gas chamber.

Quantification of the gas-phase products was performed by GC (Fuli GC9790 Plus) using a flame ionization detector for CO detection and thermal conductivity detector for H_2 detection. The liquid products were quantified by ^{1}H NMR spectroscopy using dimethyl sulfoxide (DMSO) as an internal standard.

The FE of the gas products was calculated as follows:

$$FE = \frac{Q_x}{Q_{tot}} \times 100\% = \frac{(\frac{v}{60 \text{ s min}^{-1}}) \times (\frac{y}{24000 \text{ cm}^3 \text{ mol}^{-1}}) \times N \times F}{j} \times 100\%$$

where v is the CO_2 flow rate (20 mL min^{-1}); y is the concentration of CO in a 1-mL quantitative loop (ppm); N is the electron transfer number, which is equal to 2 for CO and H_2; F is the Faraday constant (96485 C mol^{-1}); and j is the total current density (A cm^{-2}).

4. Computational procedure

The plane-wave Vienna Ab-initio Simulation Package (VASP) was applied in all first-principles calculations using projector augmented-wave pseudopotentials with the **GGA**-type PBE functional.[3,4] A model with periodic boundary conditions was used, and the plane wave energy cutoff was set to 450 eV. The reciprocal space for all calculation systems was a Monkhorst–Pack k-point grid with dimensions of 4×4×1. To prevent interactions between replicas along the z-direction, vacuum spacing of at least 20 Å was used between the adjacent images.

The binding energies (E_b) of Ni atoms with different NC configurations were calculated via the following equation:

$$E_\mathrm{b} = E_\mathrm{substrate + Ni\ atom} - E_\mathrm{substrate} - E_{Ni\ atom}$$

The adsorption energy was calculated by the following formula:

$$E_a = E_{final} - E_{substrate} - E_{adsorbate}$$

where E_a, E_final, $E_\mathrm{substrate}$, and $E_\mathrm{adsorbate}$ are the adsorption energy of the adsorbate on the substrate, total energy of the adsorbate on the substrate, total energy of the substrate, and total energy of the adsorbate, respectively.

The free energy of this reaction was computed via the following equation: $\Delta G = E_\mathrm{a} + \Delta ZPE - T\Delta S$, where ΔG, ΔZPE, and ΔS represent the Gibbs free energy, zero-point energy, and entropy, respectively.
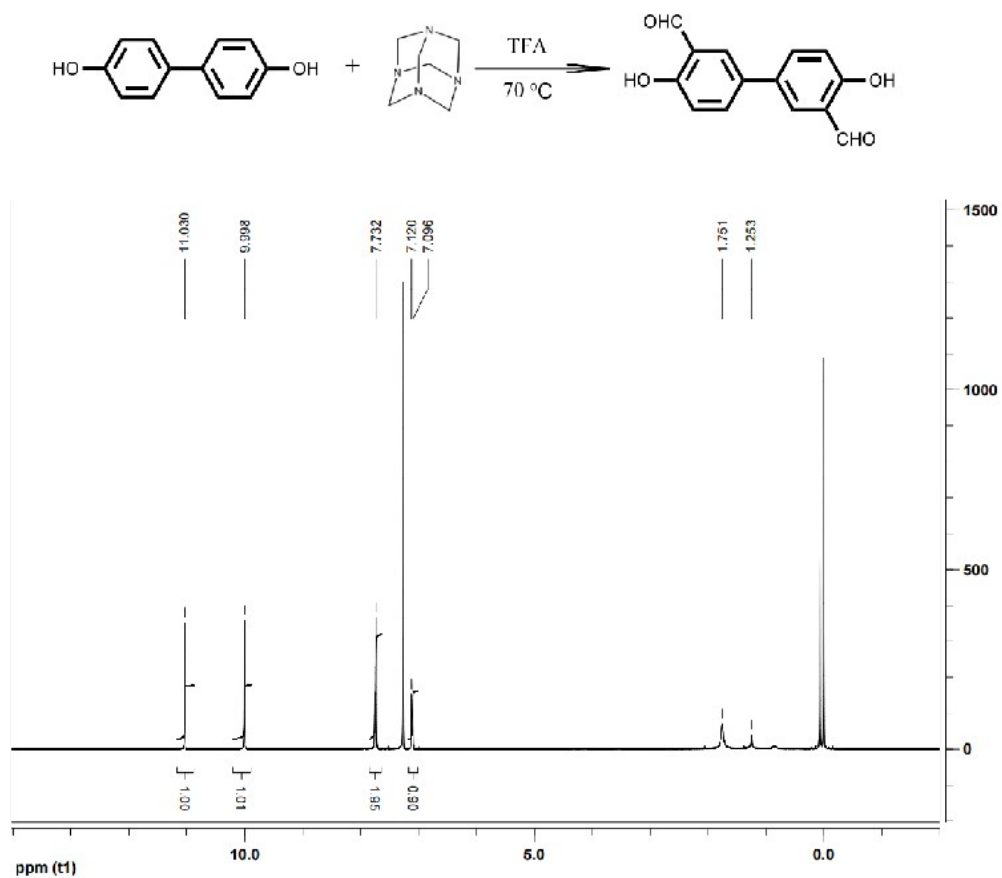
Fig. S1. Synthesis and ^{1}H NMR spectrum of 3,3'-dialdehyde-4,4'-dihydroxybiphenyl.
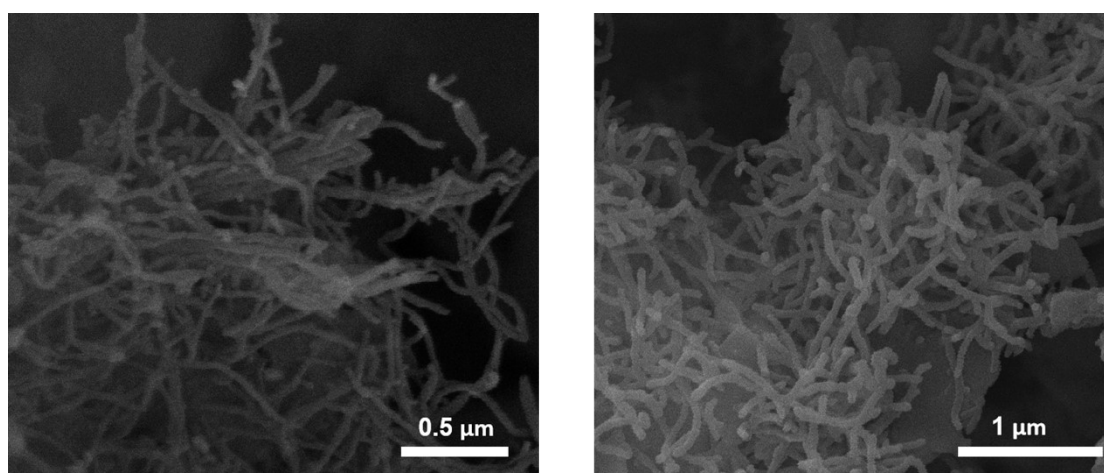
Fig. S2. SEM images of Ni-salen polymer.
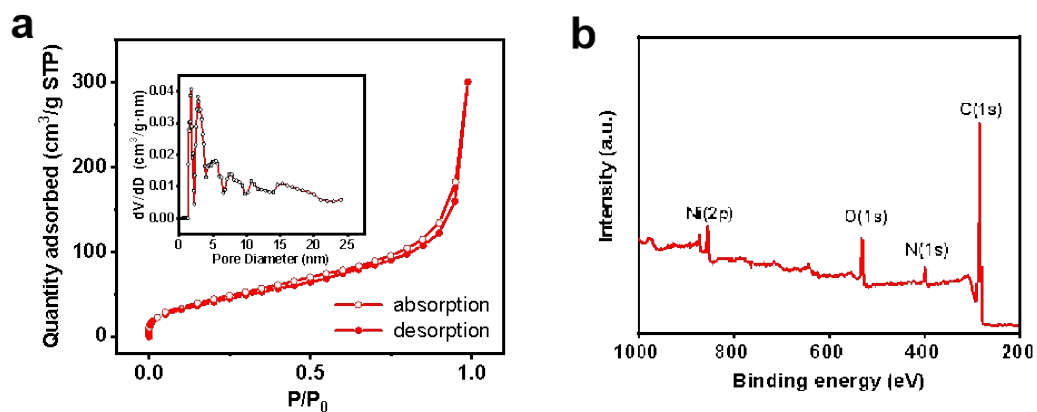
Fig. S3. (a) N_2 adsorption–desorption isotherms and the corresponding pore size distribution of Ni-salen polymer; (b) XPS profile of Ni-salen polymer.
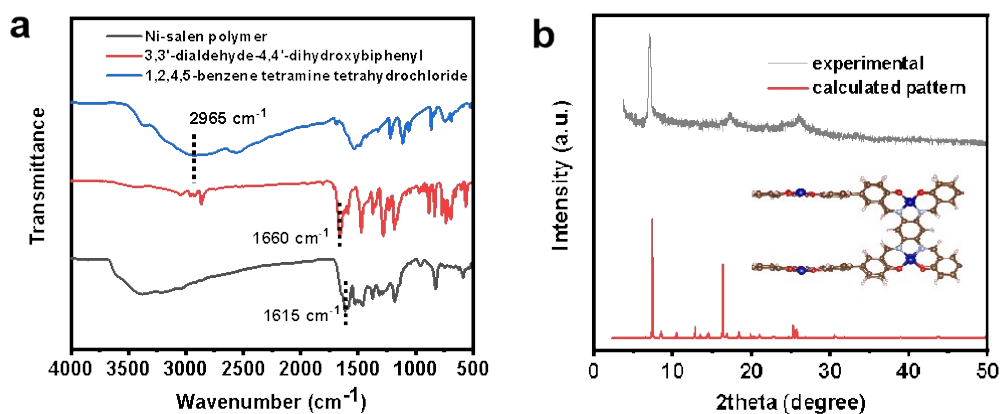
Fig. S4. (a) FT-IR spectra of raw materials and Ni-Salen polymer; (b)XRD pattern of Ni-salen polymer.
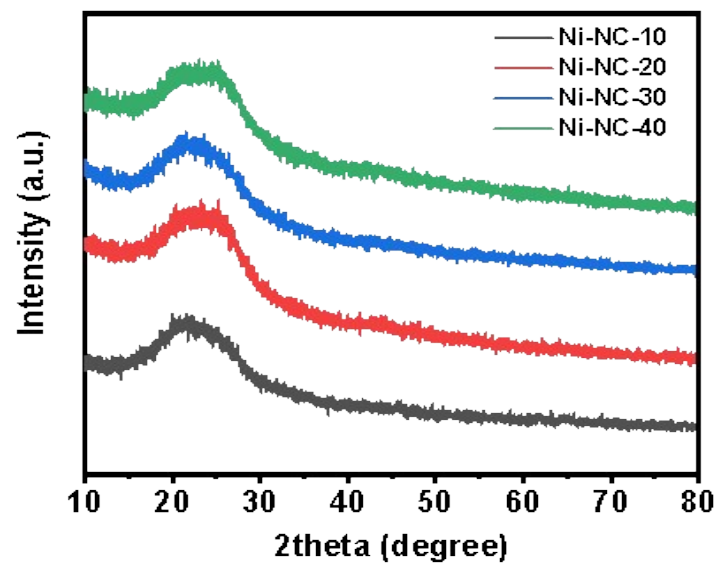
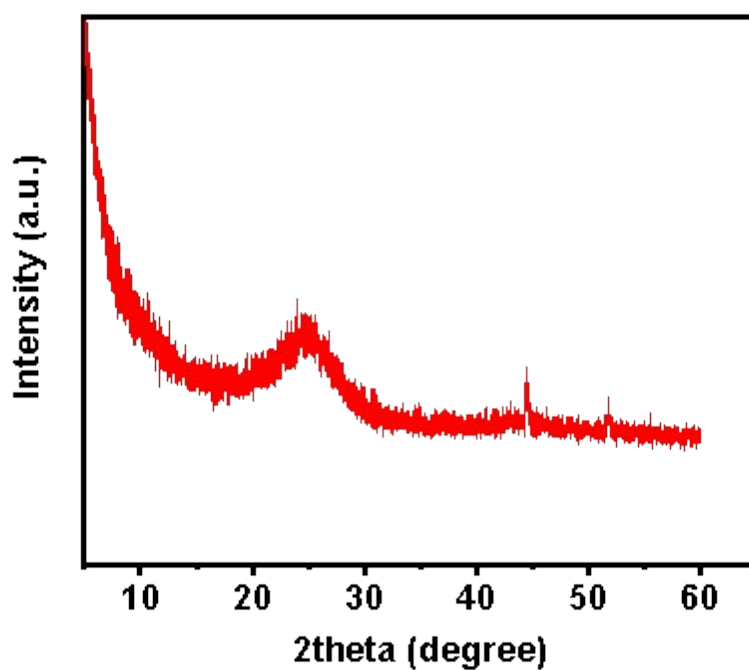**Fig. S5.** XRD patterns of Ni-NC-10, Ni-NC-20, Ni-NC-30 and Ni-NC-40.

Figure S6. XRD pattern of Ni–NC-60.
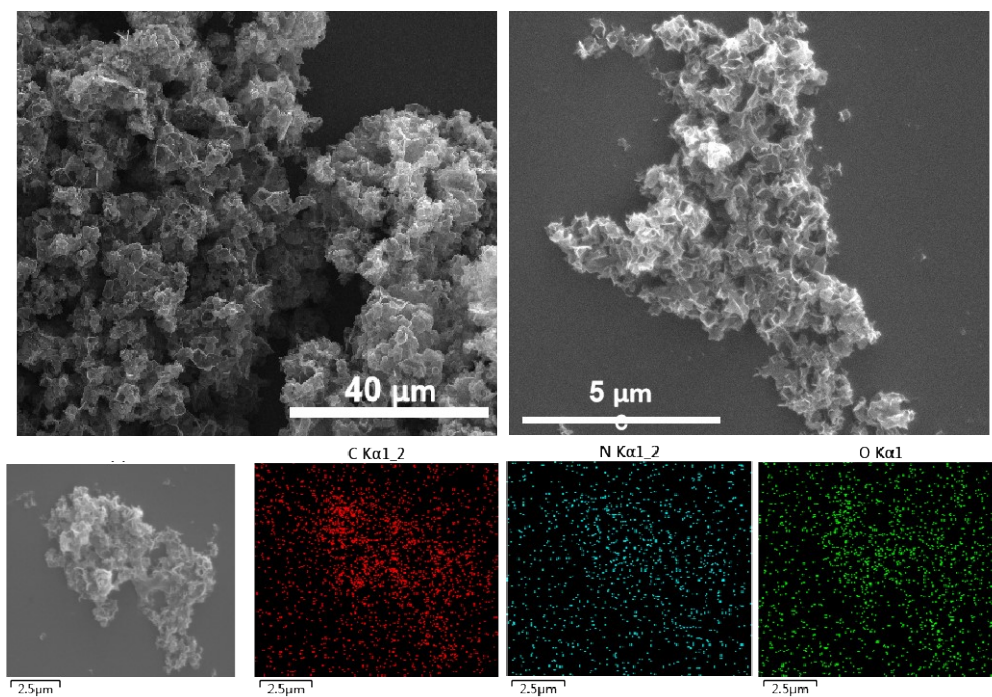
Fig. S7. SEM images and energy dispersive X-ray spectroscopy (EDS) maps of NC.
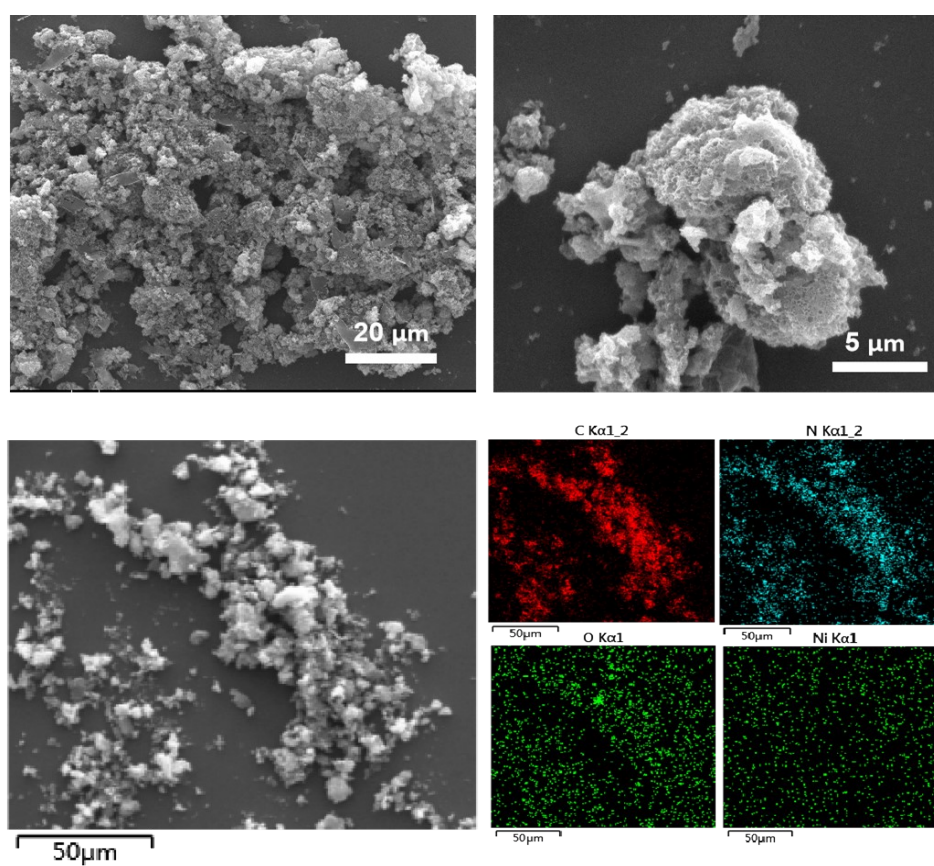
Fig. S8. SEM images and EDS maps of Ni–NC-10.
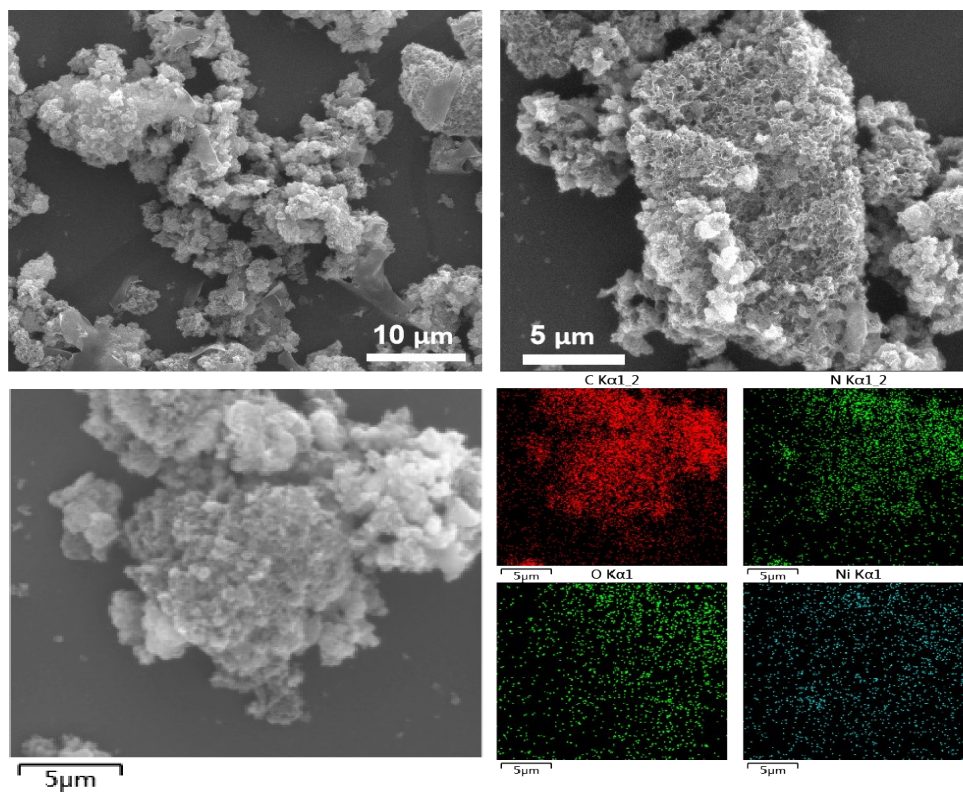
Figure S9. SEM images and EDS maps of Ni–NC-20.
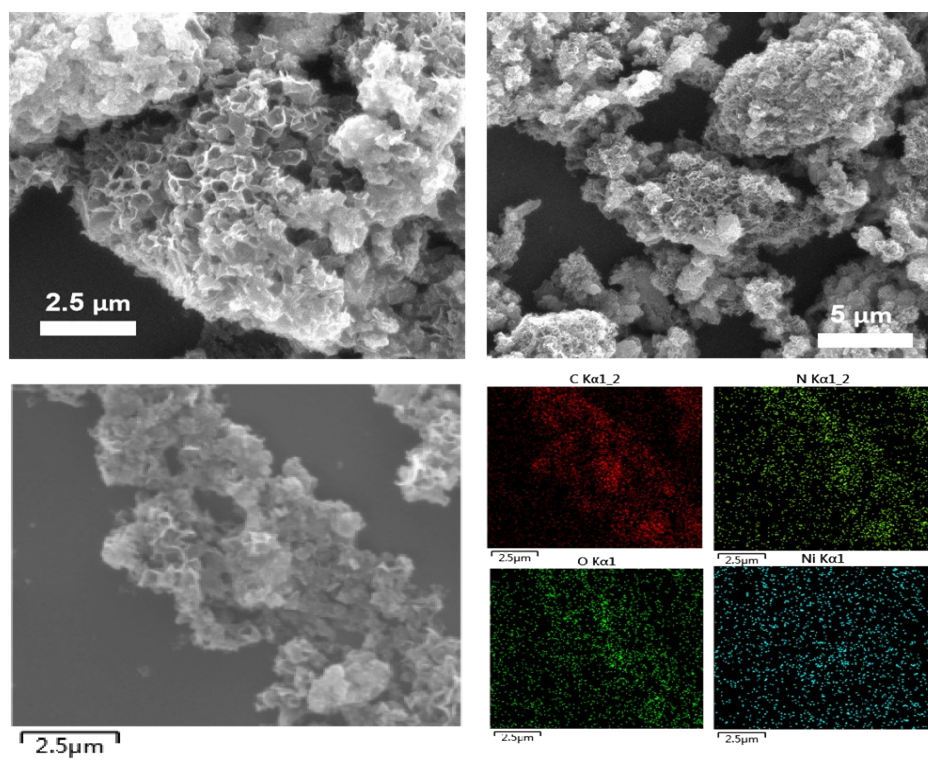
Fig. S10. SEM images and EDS maps of Ni–NC-30.
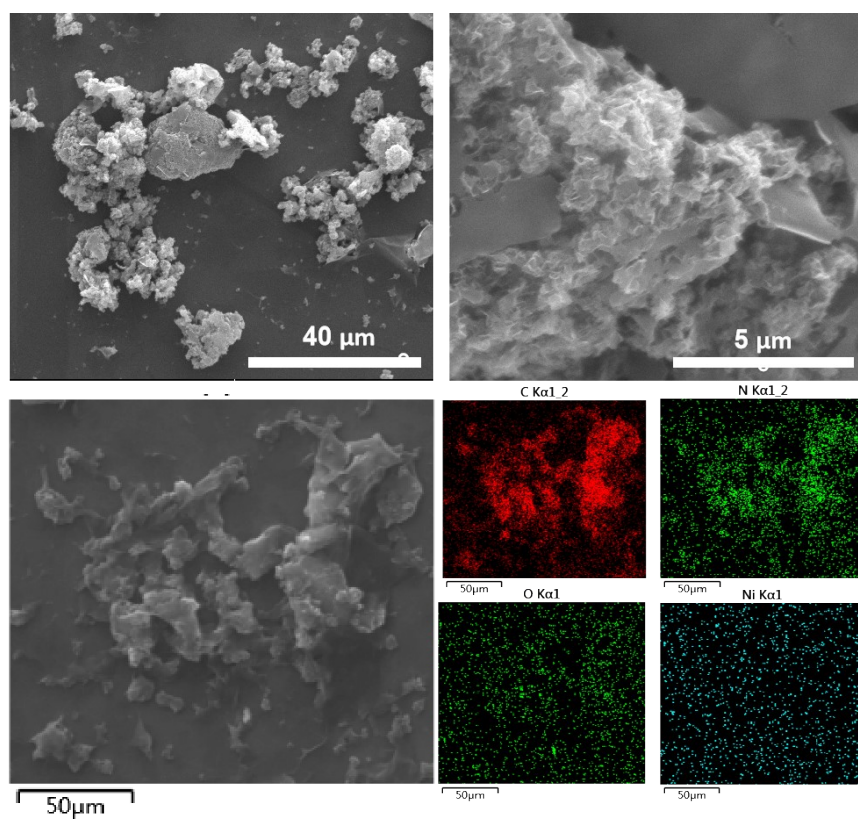
Fig. S11. SEM images and EDS maps of Ni–NC-40.
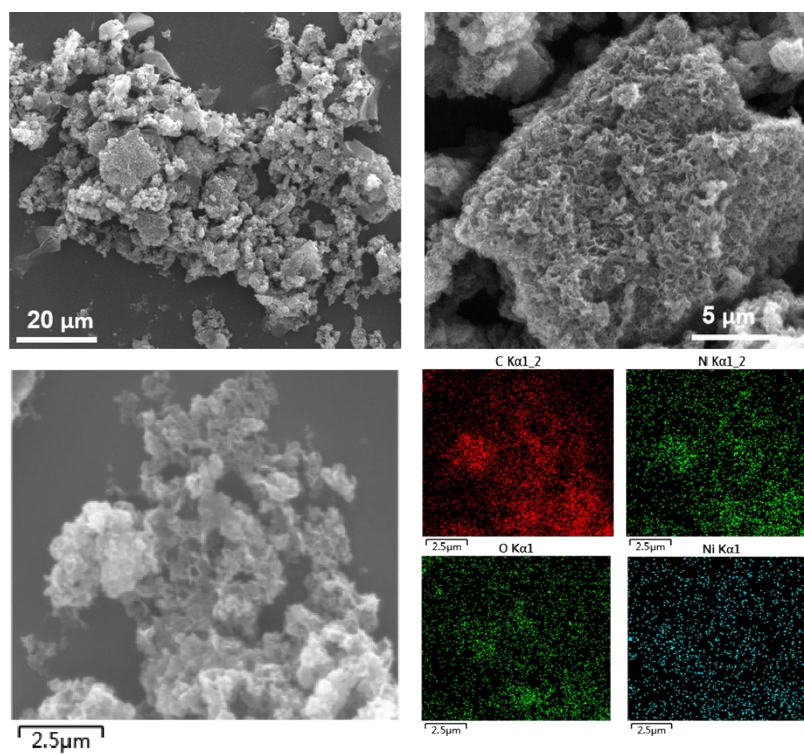
Fig. S12. SEM images and EDS maps of Ni–NC-50.
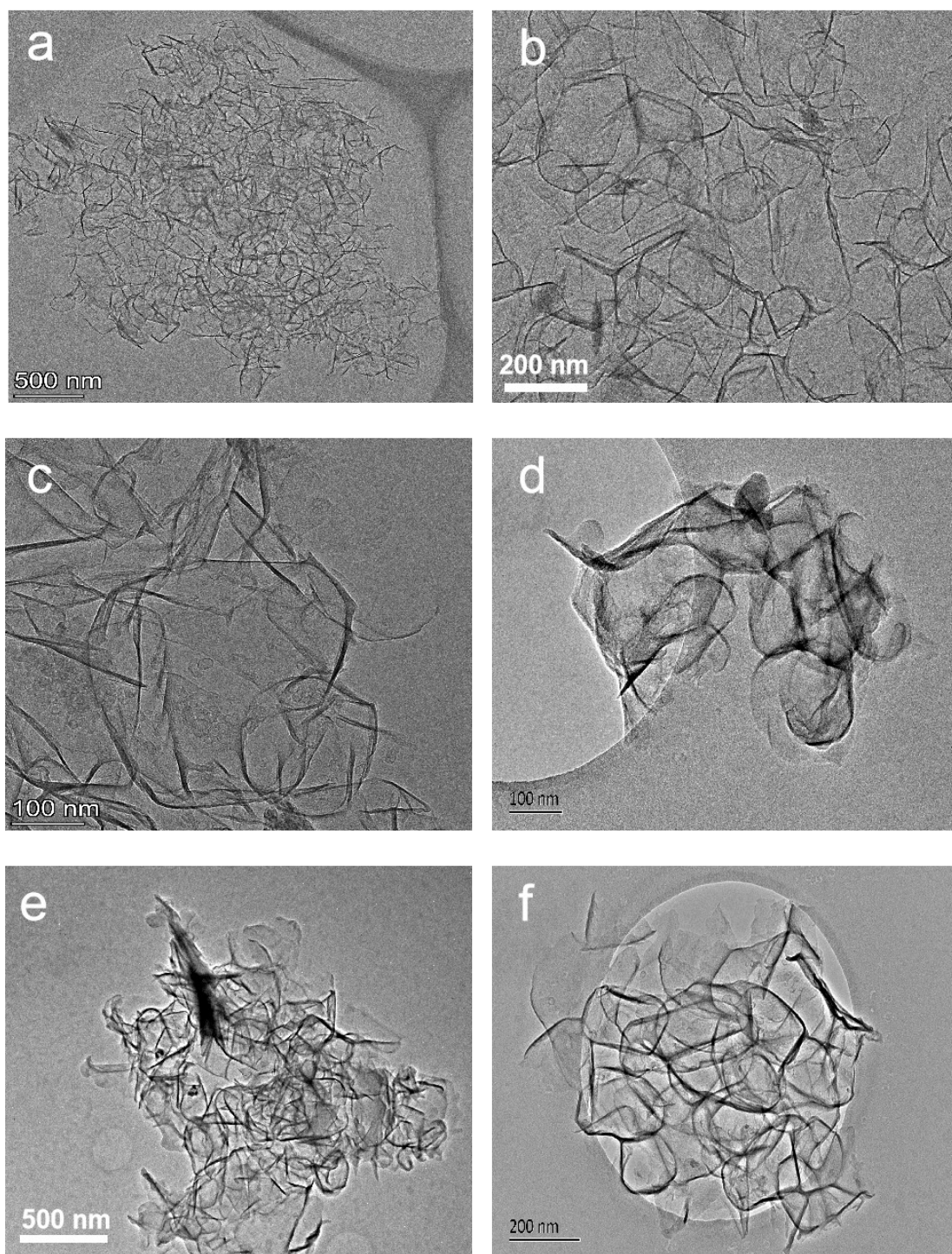
Fig. S13. TEM images of (a) NC, (b) Ni–NC-10, (c) Ni–NC-20, (d) Ni–NC-30, (e) Ni–NC-40, and (f) Ni–NC-50.
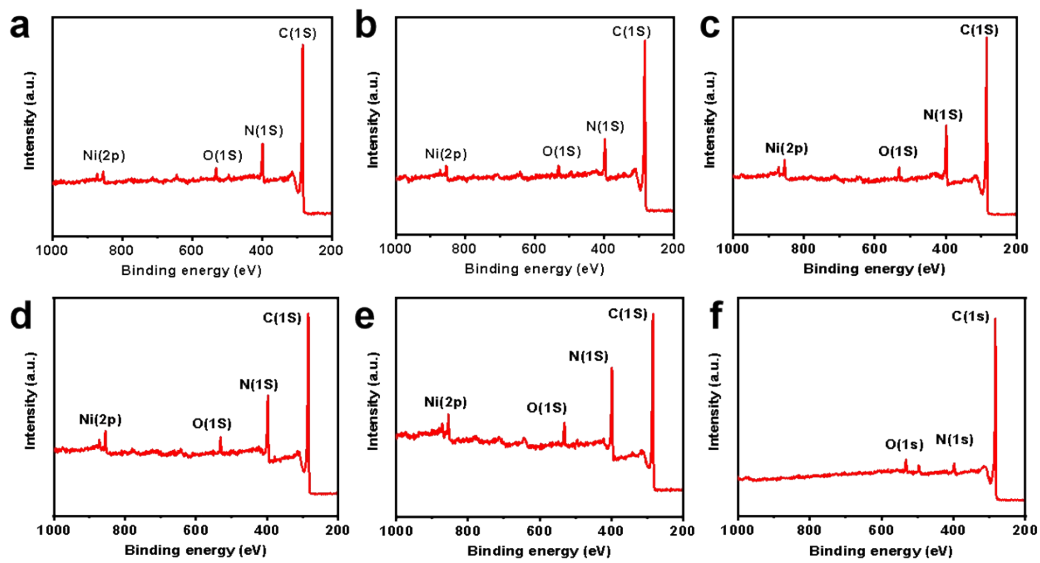
Fig. S14. XPS profiles of (a) Ni–NC-10, (b) Ni–NC-20, (c) Ni–NC-30, (d) Ni–NC-40, (e) Ni–NC-50, and (f) NC.
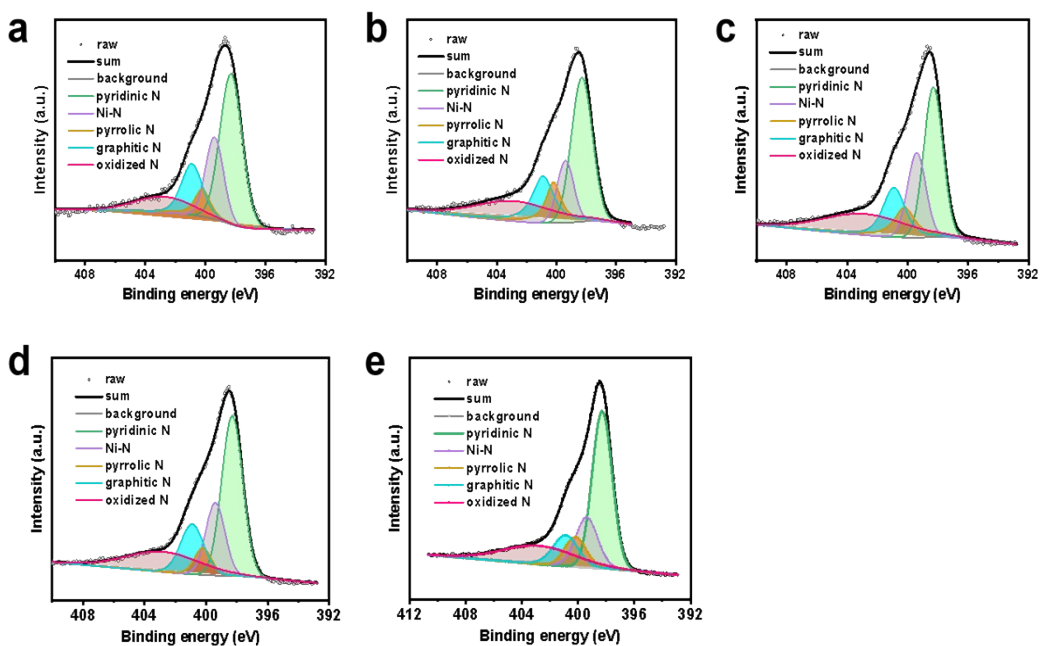
Fig. S15. High-resolution N 1s XPS profiles of (a) Ni–NC-10, (b) Ni–NC-20, (c) Ni–NC-30, (d) Ni–NC-40, and (e) Ni–NC-50.
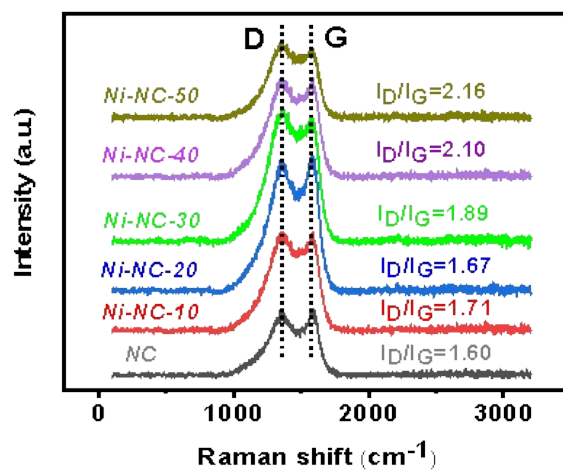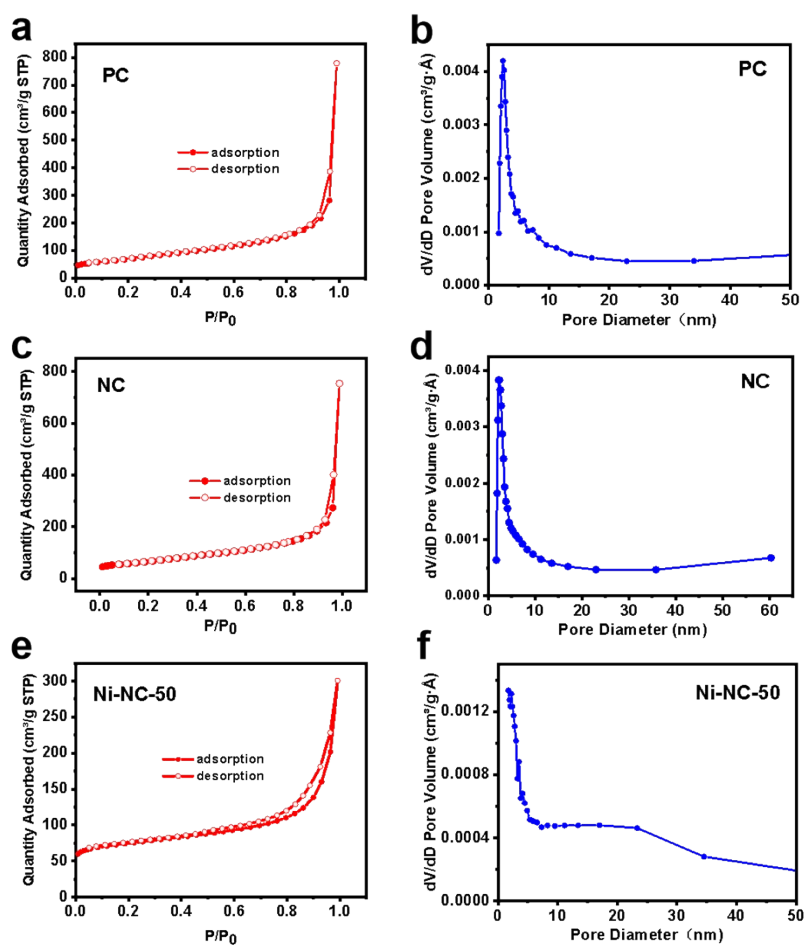
Fig. S16. Raman spectra of various catalysts.

Fig. S17. (a, c, and e) N_2 adsorption–desorption isotherms and (b, d, and f) the corresponding pore size distributions of PC, NC, and Ni–NC-50.
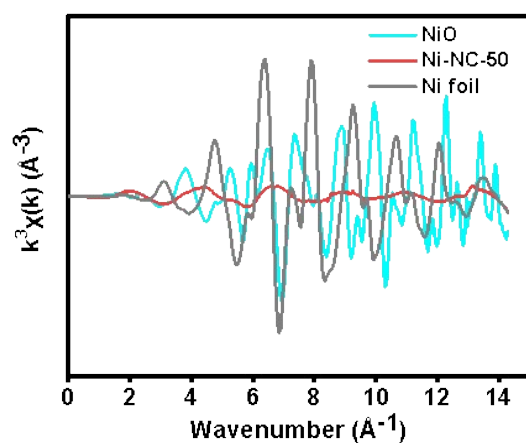
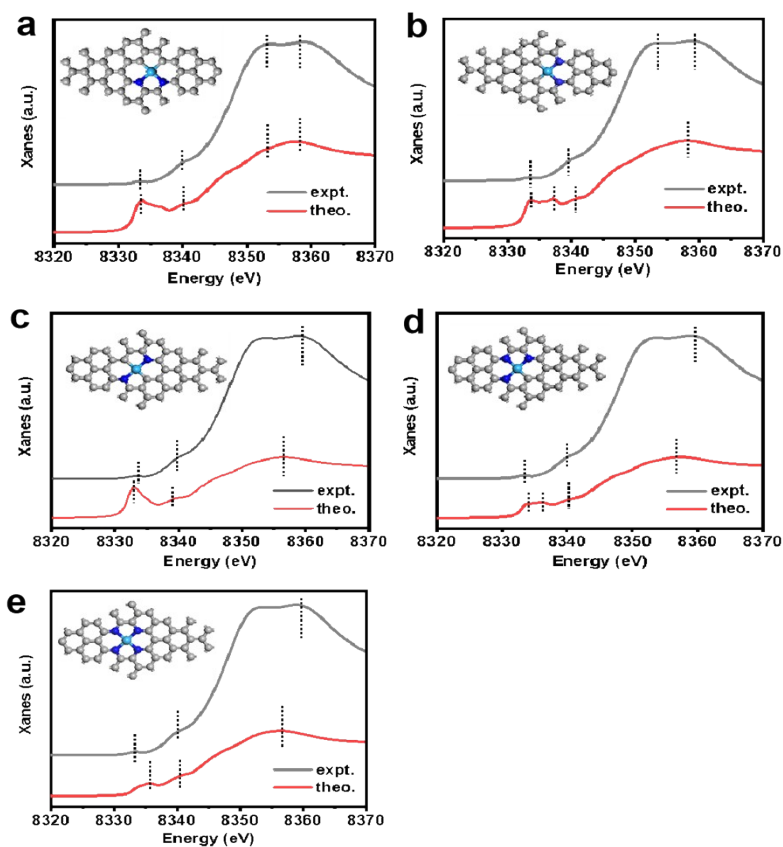**Fig. S18.** $k^3 \chi(k)$ oscillations of the Ni K-edge EXAFS.

Fig. S19. Comparison between the experimental K-edge XANES spectra and the theoretical spectra of (a)Ni–N_2C_2-p, (b) Ni–N_2C_2-h, (c) Ni–N_2C_2-o, (d) Ni–N_3C, (e) Ni–N_4.
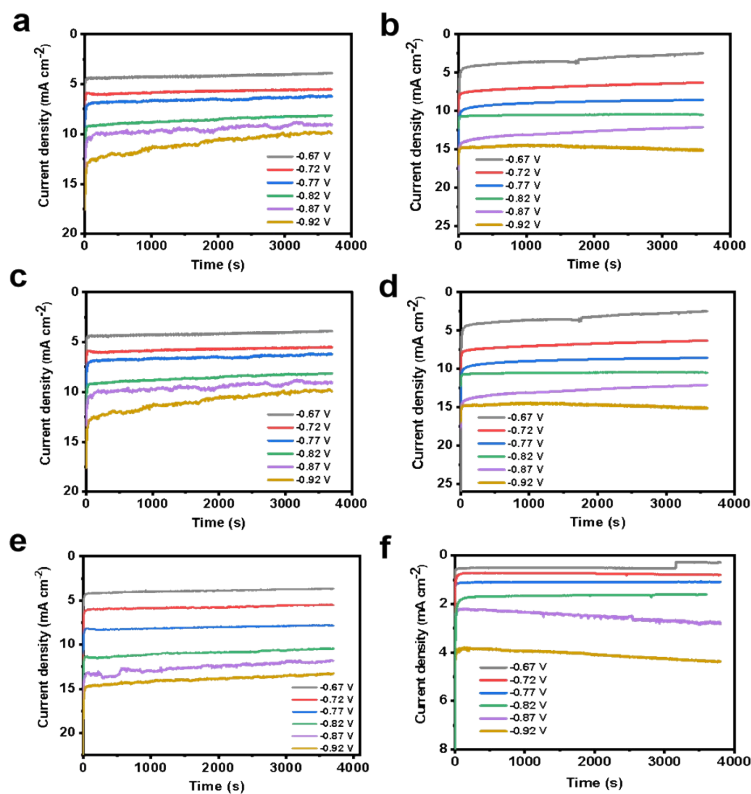
Figure S20. Results of the continuous chronoamperometric experiments conducted in the 0.5 M KHCO₃ solution saturated with pure CO_2 for CO₂RR at different applied potentials on (a) Ni–NC-10, (b) Ni–NC-20, (c) Ni–NC-30, (d) Ni–NC-40, (e) Ni–NC-50, and (f) NC.
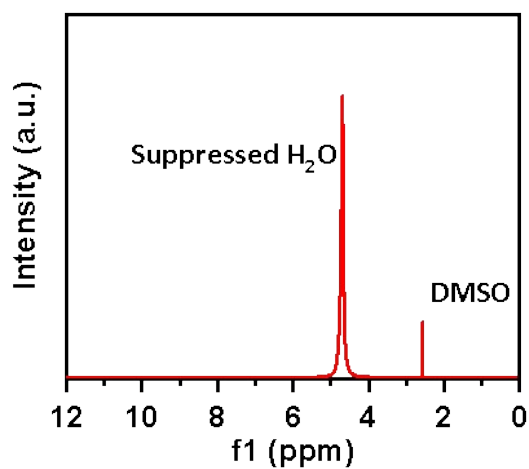

Figure S21. ¹H-NMR spectrum of the potential liquid products obtained for Ni–NC-50 in the CO₂-saturated 0.5 M KHCO₃ electrolyte after a constant potential electrolysis.
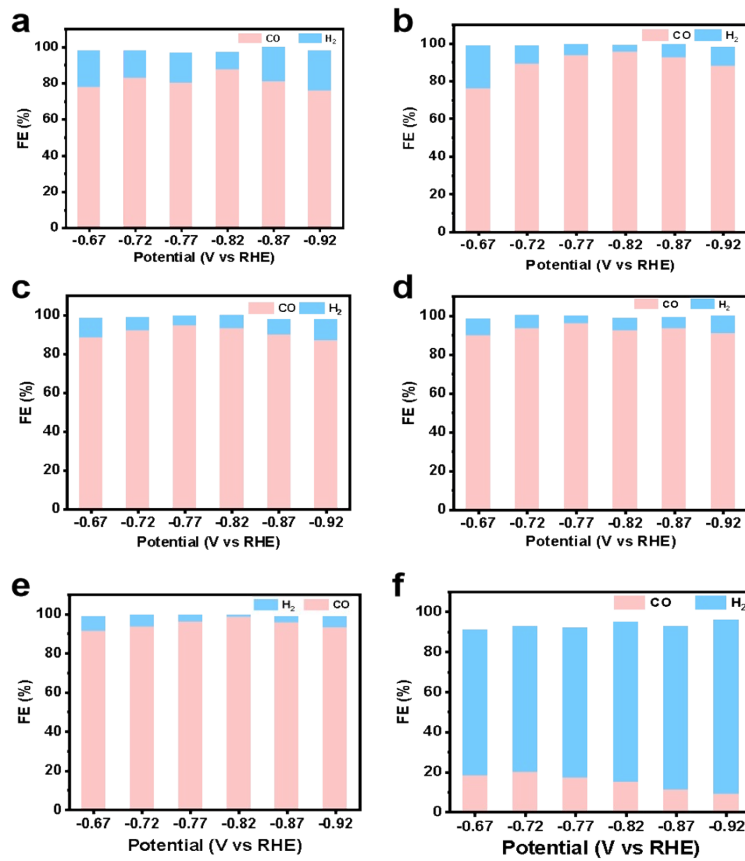
Figure S22. FEs of (a) Ni–NC-10, (b) Ni–NC-20, (c) Ni–NC-30, (d) Ni–NC-40, (e) Ni–NC-50, and (f) NC in the 0.5 M KHCO₃ electrolyte saturated with pure CO₂.
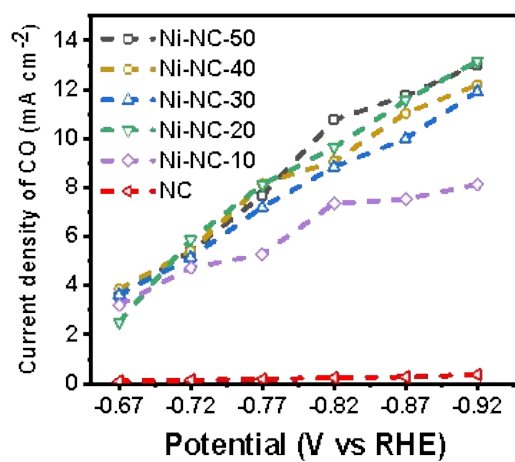

Figure S23. Current densities of CO measured at different applied potentials.
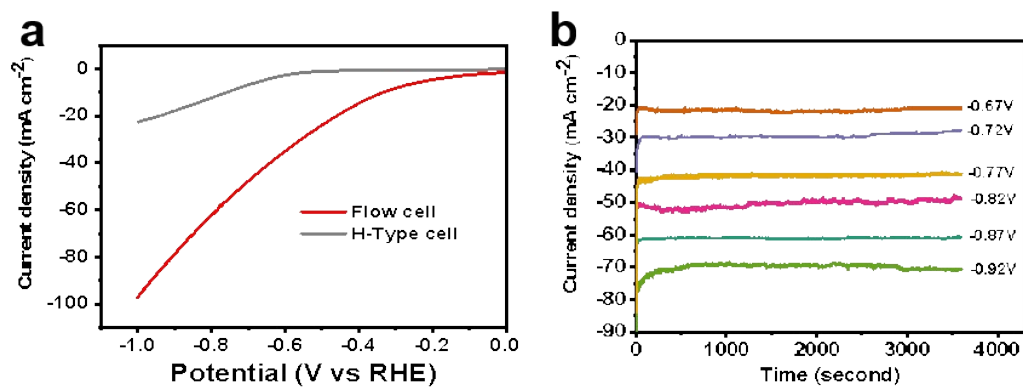
Figure S24. (a) LSV curves and (b) the chronoamperometric current–time (i–t) curves of Ni-NC-50 measured in the flow cell.
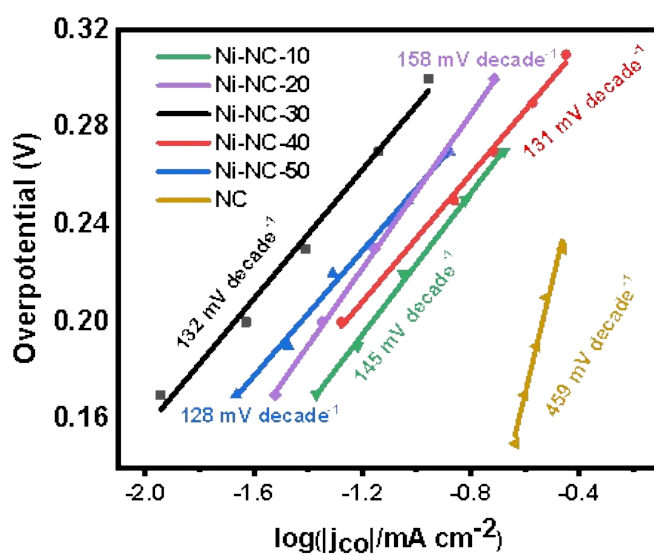

Figure S25. Tafel plots of Ni–NC-10, Ni–NC-20, Ni–NC-30, Ni–NC-40, Ni–NC-50, and NC.
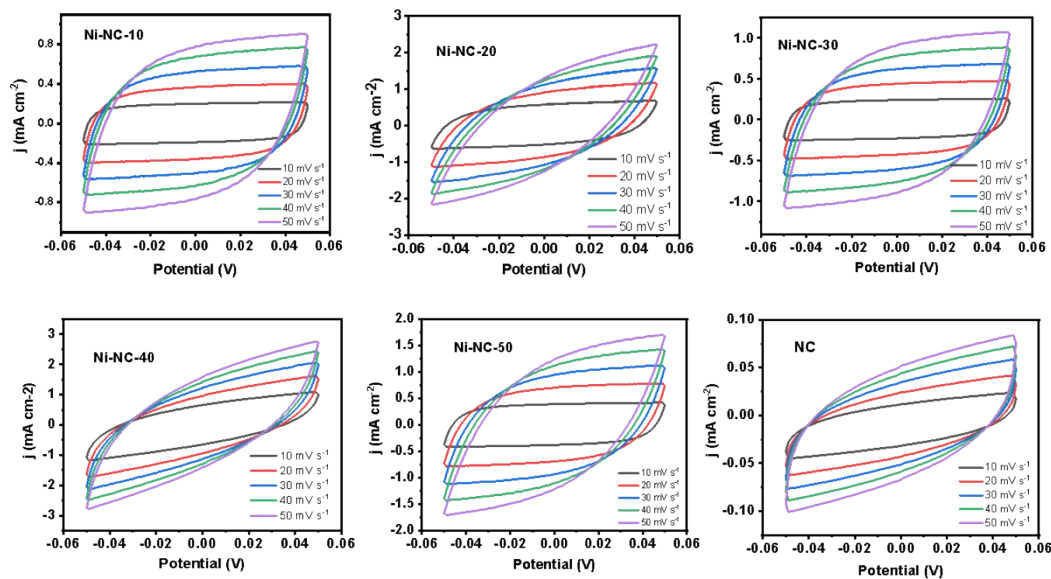
Figure S26. Cyclic voltammetry curves of Ni–NC-10, Ni–NC-20, Ni–NC-30, Ni–NC-40, Ni–NC-50, and NC recorded in the potential range from −0.05 to 0.05 V vs. RHE at scan rates of 10–50 mV s^{-1}.
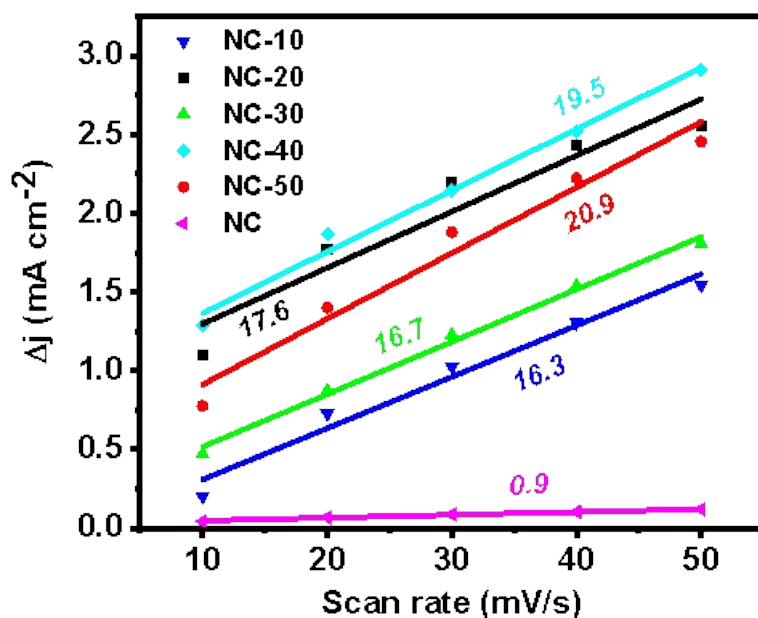

Figure S27. Double layer capacities of Ni–NC-10, Ni–NC-20, Ni–NC-30, Ni–NC-40, Ni–NC-50, and NC.
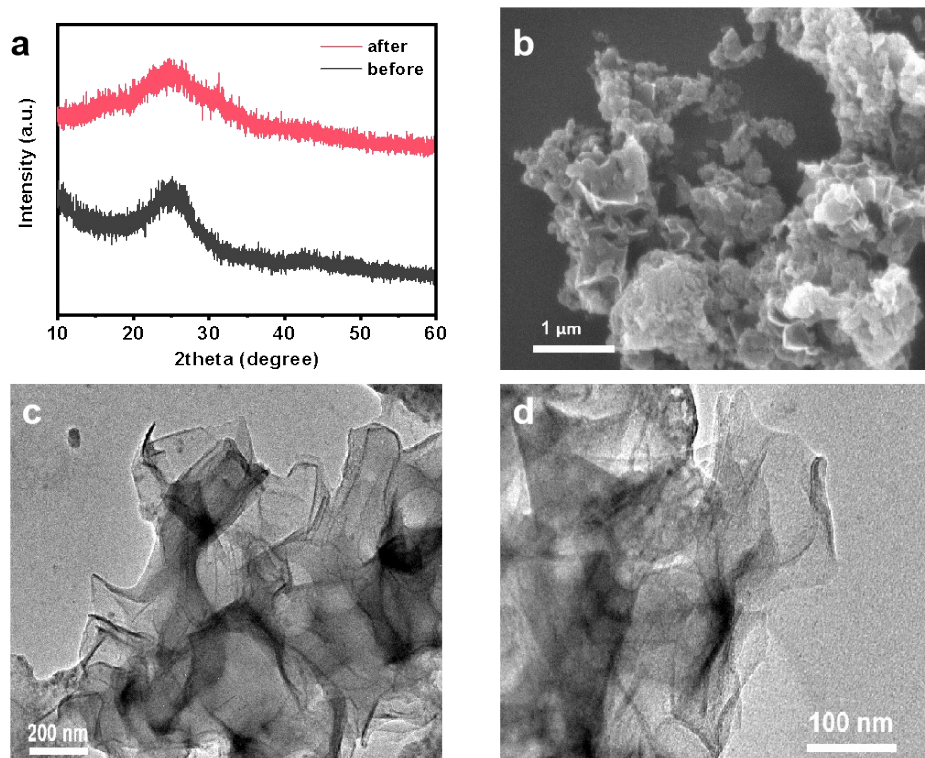
Figure S28. (a) XRD pattern, (b) SEM image, and (c, d) TEM images of the Ni–NC-50 catalyst obtained after the CO$_2$RR stability test.
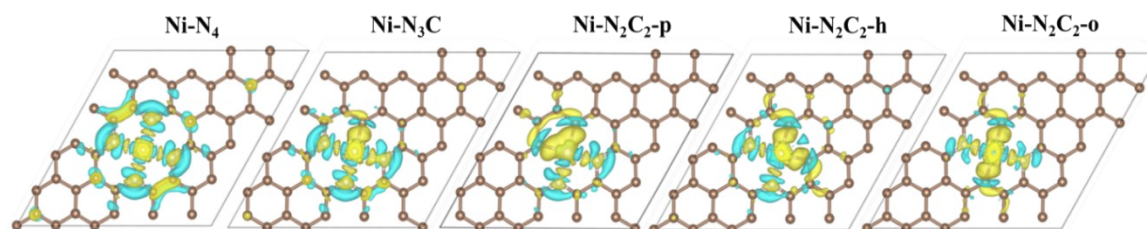

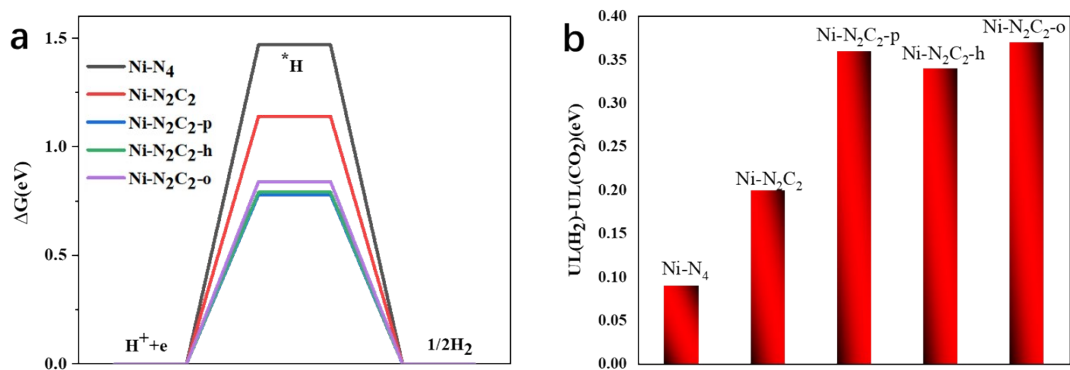**Figure S29**. Charge density differences of the five Ni SAC models.

Figure S30. Calculated (a) free energy diagrams for the HER and (b) differences between the limiting potentials of the CO$_2$RR and HER conducted on the five Ni SAC models.
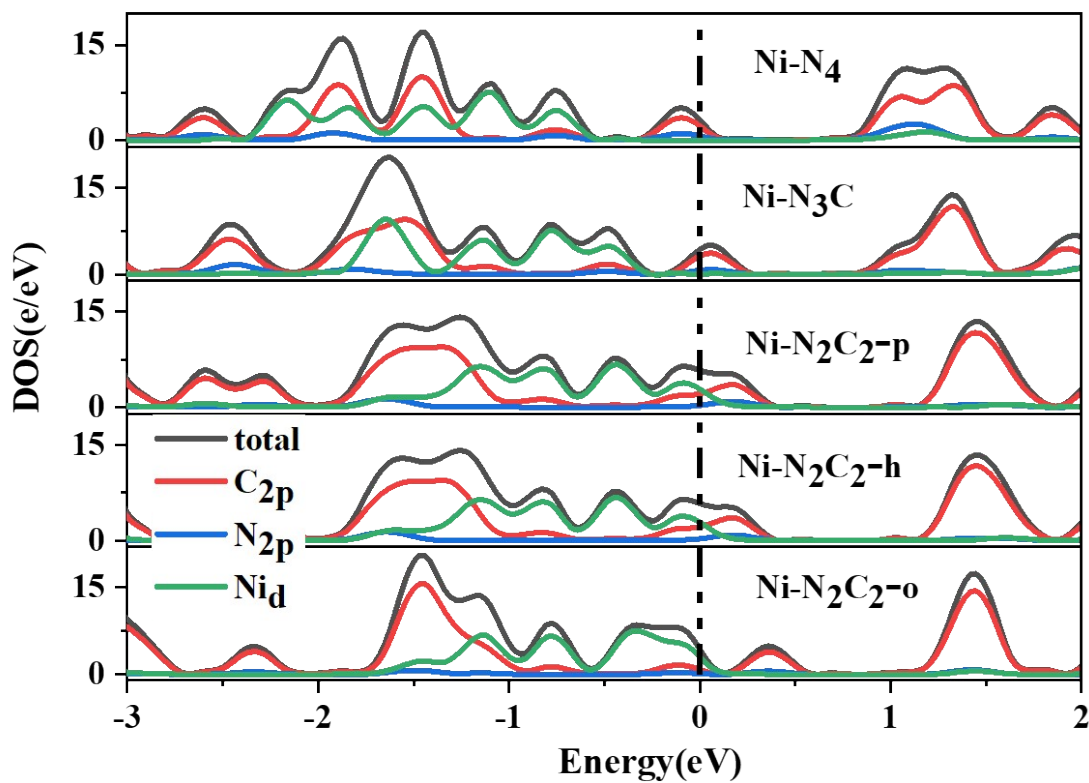

Figure S31. The TDOS and PDOS of five Ni SACs models.

Table S1. Summary of element content (wt.%) analyzed by XPS and ICP.

sample	N (by XPS)	O (by XPS)	Ni (by ICP)
NC	5.6	5.3	0
Ni-NC-10	12.0	4.0	5.26
Ni-NC-20	13.4	4.1	6.38
Ni-NC-30	16.9	3.8	7.19
Ni-NC-40	18.2	4.1	8.10
Ni-NC-50	23.5	4.5	9.15

Table S2. Summary of metal content of some Ni SACs.

Catalyst	Metal precursors	Metal content (wt%)	Reference
Ni-NC-50	Ni-salen polymer	9.15	This work
Ni$_1$-N-C	MTV-MOFs	1.75	Angew. Chem. Int. Ed., 2020, 59, 20589
Ni-hG	Holey graphene (hG) framework	2.0	ACS nano, 2021, 15, 12006
Ni-NC	NiCl$_2$·6H$_2$O	1.2	Angew. Chem. Int. Ed., 2020, 59, 3033
Ni–Zn–N–C	NiCl$_2$ and ZnCl$_2$	2.16	Adv. Mater., 2021, 33, 2102212
Ni$_2$/NC	Ni$_2$(dppm)$_2$Cl$_3$ cluster	0.18	J. Am. Chem. Soc., 2021, 143, 11317
A–Ni–NSG	Melamine/l-alanine(l-cysteine)	2.8	Nat. Energy, 2018, 3, 140
Ni-NCB	Ni salts	0.27	Joule, 2019, 3, 265
Ni SACs/N-C	Ni(acac)$_2$	0.10	Nat. Commun., 2020, 11, 1
SA-Ni-NC	ZnNi-ZIF	2.39	J. Mater. Chem. A, 2022, 10, 6122
CNS-NiSA	eNiPS$_3$-Br	0.5	Carbon, 2021, 178, 488
Ni-N-C	Ni(NO$_3$)$_2$·6H$_2$O	1.08	Angew. Chem. Int. Ed., 2021, 133, 26786

Table S3. Structural parameters extracted from the EXAFS fitting.

sample	shell	N	R(Å)	$\sigma^2(10^{-3}Å^2)$	$\Delta E0$ (eV)	R-factor (%)
Ni foil	Ni-Ni	12	2.44±0.01	8±0.5	-6.8±0.7	0.6
NiO	Ni-O	6	2.08±0.02	5.3±0.8	-5.4±1.2	1.3
	Ni-Ni	12	2.95±0.01	3.9±0.2		
Ni-NC-50	Ni-C	2.3±0.2	1.90±0.01	5.4±1.1	-6.0±1.5	1.3
	Ni-N	1.7±0.3	2.07±0.02	5.4±1.1		

N, coordination number; R, distance between absorber and backscatter atoms; σ^2, Debye-Waller factor; ΔE_0, inner potential correction; R factor (%) indicates the goodness of fit.

References

1 M. W. Schneider, I. M. Oppel, M. Mastalerz, *Chem. Eur. J.*, 2012, **18**, 4156-4160.

2 K. Xu, G. Xia, D. Liu, L. Jiang, M. Wang, D. Liu, X. Lv, W. Shan, H. Wang, *J. Polym. Sci., Part A: Polym. Chem.*, 2019, **57**, 641-647.

3 G. Kresse, J. Hafner, *Phys. Rev. B*, 1993, **48**, 13115.

4 G. Kresse, J. Furthmüller, *Phys. Rev. B*, 1996, **54**, 11169.